Crystal and Magnetic Structures and Physical Properties of a New Pyroxene NaMnGe$_2$O$_6$ Synthesized under High Pressure
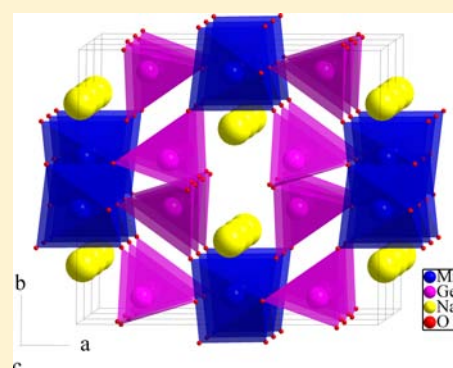
Jinguang Cheng,[†,#] Wei Tian,[‡] Jianshi Zhou,*,[†] Vincent M. Lynch,[§] Hugo Steinfink,[∥] Arumugam Manthiram,[†] Andrew F. May,[⊥] Vasile O. Garlea,[‡] Joerg C. Neuefeind,[▲] and Jiaqiang Yan*,[⊥,▽]

[†]Materials Science and Engineering Program and Texas Materials Institute, [§]Department of Chemistry and Biochemistry, and [∥]Chemical Engineering and Texas Materials Institute, The University of Texas at Austin, Austin, Texas 78712, United States
[#]Institute of Physics, Chinese Academy of Sciences, Beijing, 100190, China

[‡]Quantum Condensed Matter Division, [⊥]Materials Science and Technology Division, and [▲]Chemical & Engineering Materials Division, Oak Ridge National Laboratory, Oak Ridge, Tennessee 37831, United States
[▽]Department of Materials Science and Engineering, The University of Tennessee, Knoxville, Tennessee 37996, United States

ABSTRACT: A new pyroxene compound, NaMnGe$_2$O$_6$, has been synthesized at 3 GPa and 800 °C and fully characterized by X-ray single-crystal diffraction, neutron powder diffraction, and measurements of magnetization and specific heat. NaMnGe$_2$O$_6$ crystallizes into a monoclinic $C2/c$ structure with unit-cell parameters $a = 9.859(2)$ Å, $b = 8.7507(18)$ Å, $c = 5.5724(11)$ Å, and $\beta = 105.64(3)°$ at 153 K. A cooperative Jahn−Teller distortion is formed by an ordering of the longest Mn−O bonds between two neighboring octahedra along the chain direction. This feature distinguishes NaMnGe$_2$O$_6$ from other pyroxene compounds without Jahn−Teller active cations and suggests that the Jahn−Teller distortion competes with the intrinsic local distortion in the pyroxene structure. No orbital order−disorder transition has been found up to 750 K. Like other alkali-metal pyroxenes with $S > 1/2$, NaMnGe$_2$O$_6$ ($S = 2$) was found to undergo a long-range antiferromagnetic (AF) ordering at $T_N = 7$ K due to intrachain and interchain exchange interactions. Due to the peculiar structural features and the corresponding magnetic coupling, the weak AF spin ordering gives way to a ferromagnetic-like state at a sufficiently high magnetic field. Specific-heat measurements demonstrated that a large portion of the magnetic entropy, >60%, has been removed above T_N as a result of strong spin correlations within the quasi-one-dimensional Mn^{3+}-spin chains. The Reitveld refinement of neutron powder diffraction data gives a commensurate magnetic structure defined by $k = [0\ 0\ 0.5]$ with Mn moments aligned mainly along the c-axis with a small component along both a- and b-axes.

1. INTRODUCTION

As a common form of minerals in the Earth's crust, the pyroxene compounds have been studied extensively since the 1960s from the perspective of crystal chemistry in geology and mineralogy.[1] In recent years, the alkali-metal pyroxenes AMX$_2$O$_6$ (A = Li$^+$, Na$^+$; M = Ti^{3+}, V^{3+}, Cr^{3+}, Mn^{3+}, and Fe^{3+}; X = Si^{4+}, Ge^{4+}) have received renewed interest in the materials science community because they exhibit intriguing quasi-one-dimensional (Q1D) magnetism and multiferroic phenomena;[2] these properties are associated with the particular arrangement of the magnetic M^{3+} ions in the structure. In the monoclinic crystal structure, the edge-shared MO$_6$ octahedra form skew chains running along the crystallographic c axis (see Figure 1). Since these MO$_6$ octahedral chains are well-separated by nonmagnetic XO$_4$ tetrahedra, the intrachain magnetic interactions are considered to be much stronger than the interchain interactions, which leads to a typical Q1D spin-chain system. Within the zigzag chains of MO$_6$ octahedra, the edge-sharing octahedra provide a 90° M−O−M pathway for superexchange interactions. Interestingly, the magnetic coupling

in pyroxenes can be altered by either the orbital occupation on the M site or a chemical substitution on the A site. The continuous variation of the d-orbital occupancy by substituting different transition-metal ions at the M^{3+} site makes their magnetic properties extremely rich in this family. Streltsov and Khomskii[3] have performed theoretical analysis and ab initio simulations on the electronic structures and magnetic properties for all (Li,Na)M(Si,Ge)$_2$O$_6$ pyroxenes with M = Ti^{3+} (d^1), V^{3+} (d^2), Cr^{3+} (d^3), Mn^{3+} (d^4), and Fe^{3+} (d^5) that the pyroxene structure can accommodate so far, and their work reveals that there is a competition between antiferromagnetism and ferromagnetism on the 90° Mn−O−Mn bond in the Mn-based pyroxene. This prediction has not been confirmed experimentally. In Table 1, we have included the crystal structure and magnetic properties of known pyroxenes (Li,Na)M(Si,Ge)$_2$O$_6$ (M = Ti, V, Cr, Mn, and Fe). As a system with S = 1/2 spin-chains, the Ti-based pyroxenes ATiSi$_2$O$_6$ were found to undergo a spin-Peierls transition at
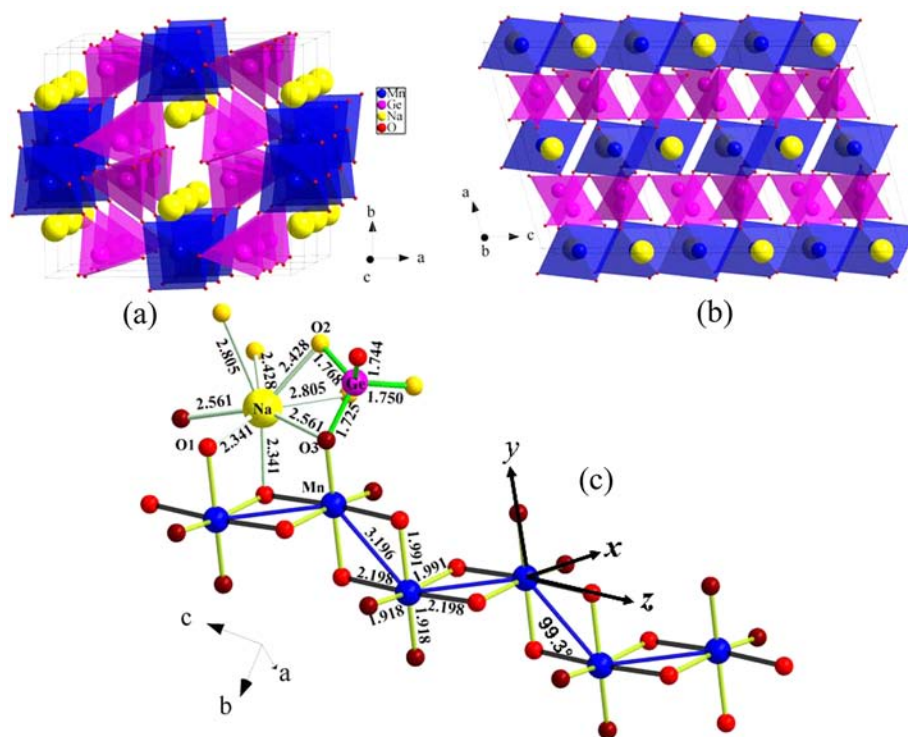
Figure 1. Crystal structure of NaMnGe$_2$O$_6$: (a) projected along the c axis; (b) along the b axis; (c) schematic drawing of octahedra along the direction of chains and surrounding polyhedra.

Table 1. Summary of Crystal Structure and Magnetic Properties of (Li,Na)M(Si,Ge)$_2$O$_6$ Pyroxenes[a]

compd	space group[b]	lattice parameters[b]				magnetic structure		physical properties	refs
		a, Å	b, Å	c, Å	β, deg	intrachain	interchain		
LiTiSi$_2$O$_6$	C2/c	9.66	8.73	5.30	109.8			spin-Peierls-like transition below T_s = 230 K	4,5
NaTiSi$_2$O$_6$	C2/c	9.692	8.874	5.301	106.85			spin-Peierls-like transition below T_s = 210 K	4,5
LiVSi$_2$O$_6$	C2/c	9.634	8.586	5.304	109.69			AFM below T_N = 22 K, max $\chi(T)$ at T_m = 110 K	16−18,48
NaVSi$_2$O$_6$	C2/c	9.634	8.741	5.296	106.91			AFM below T_N = 17 K, max $\chi(T)$ at T_m = 48 K	16,17,49
LiVGe$_2$O$_6$	P2$_1$/c	9.851	8.754	5.395	108.0	AFM	FM	AFM below T_N = 24 K, max $\chi(T)$ at T_m = 60 K	9,11−13,16,39
NaVGe$_2$O$_6$	C2/c	9.960	8.853	5.486	106.40			AFM below T_N = 16 K, max $\chi(T)$ at T_m = 26 K	14−16,39
LiCrSi$_2$O$_6$	P2$_1$/c	9.536	8.581	5.249	109.93	AFM	FM	AFM below T_N = 11 K, max $\chi(T)$ at T_m = 19 K, multiferroic	2,20,21
NaCrSi$_2$O$_6$	P2$_1$/c	9.51	8.67	5.24	107.3			AFM below T_N = 3 K, max $\chi(T)$ at T_m = 3.6 K	19,20
LiCrGe$_2$O$_6$	P2$_1$/c	9.799	8.719	5.341	108.91			AFM below T_N = 3.7 K, max $\chi(T)$ at T_m = 5.2 K	20,38
NaCrGe$_2$O$_6$	C2/c	9.915	8.844	5.460	107.55	FM	FM	FM below T_c = 6 K	19,20,22,38
NaMnSi$_2$O$_6$	C2/c	9.513	8.621	5.354	105.14				29
NaMnGe$_2$O$_6$	C2/c	9.859	8.751	5.572	105.64	up−up−down−down	FM	AFM below T_N = 7 K	this work
LiFeSi$_2$O$_6$	C2/c	9.664	8.661	5.292	110.12	FM	AFM	AFM below T_N = 18 K, max $\chi(T)$ at T_m = 20 K, multiferroic	2,23,28,50
NaFeSi$_2$O$_6$	C2/c	9.68	8.83	5.30	107.3	FM	AMF	AFM below T_N = 8 K, multiferroic	2,24,28
LiFeGe$_2$O$_6$	P2$_1$/c	9.873	8.795	5.372	106.92	AFM	AFM/FM	AFM below T_N = 20 K, max $\chi(T)$ at T_m = 24 K	25,50
NaFeGe$_2$O$_6$	C2/c	10.008	8.948	5.523	107.59	IC-AFM		AFM below T_N = 15 K, max $\chi(T)$ at T_m = 25 K	26,27

[a] M = Ti, V, Cr, Mn, and Fe. AFM, antiferromagnetism; FM, ferromagnetism; $\chi(T)$, paramagnetic susceptibility. [b] At room temperature.

T_s = 230 K for A = Li and at T_s = 210 K for A = Na,[4] which is accompanied by the formation of Ti−Ti dimers below T_s.[5] These observations are consistent with a spin-singlet ground state driven by the orbital ordering of Ti^{3+} (d^1) ions.[6−8] In contrast to the half-integer spin chains in (Li,Na)TiSi$_2$O$_6$, the V-based pyroxenes have been considered as a promising 1D Haldane-chain system with

integer spin S = 1.[9,10] However, all V-based pyroxenes were observed to form a long-range antiferromagnetic (AFM) ordered state below T_N = 16−24 K due to relatively strong interchain exchange interaction.[11−16] Nevertheless, their magnetic susceptibility $\chi(T)$ curves all exhibit a Bonner−Fisher-like broad maximum at a temperature $T_m \gg T_N$, which is characteristic of Q1D

magnetic compounds.[16−18] As the total spin becomes larger, this feature in $\chi(T)$ transforms into a sharp cusplike anomaly with T_m very close to T_N. More interestingly, the magnetic ground state of Cr-based pyroxenes evolves from the long-range AFM order for LiCr(Si,Ge)$_2$O$_6$ to ferromagnetic (FM) order for NaCrGe$_2$O$_6$ as a result of the competition between FM t$_{2g}$−e$_g$ and AFM t$_{2g}$−t$_{2g}$ superexchange interactions.[19,20] At the crossover, NaCrSi$_2$O$_6$ was found to undergo a magnetic-field-driven spin-flip transition from an AFM to a FM state.[20] The magnetic structure of LiCrSi$_2$O$_6$ is commensurate with the chemical unit cell and is characterized by AFM coupling within the CrO$_6$ octahedral chains and FM coupling between the chains,[21] while the magnetic structure of NaCrGe$_2$O$_6$ features one-dimensional FM magnetic chains spin-aligned along the c axis of the monoclinic cell.[22] As for Fe-based pyroxenes (Li,Na)Fe(Si,Ge)$_2$O$_6$, they all undergo long-range AFM order at low temperatures.[23−27] The renewed interest in this latter class of compounds arises from the recent observation of magnetically driven ferroelectricity in the magnetically ordered state of (Li,Na)FeSi$_2$O$_6$.[2,28] Although it remains controversial, the possibility of an incommensurate or spiral magnetic structure has been proposed as the origin of the multiferroic behavior in the iron pyroxenes.[2,27]

The previously studied magnetic AMX$_2$O$_6$ compounds listed in Table 1 have M^{3+} ions that are either weakly Jahn−Teller (JT) -active for M^{3+} = Ti^{3+} (3d^1) or V^{3+} (3d^2) or non-JT-active for M^{3+} = Cr^{3+} (3d^3) or Fe^{3+} (3d^5). A cooperative long-range orbital ordering normally in a system with the JT-active ions leads to structural distortions on top of the intrinsic structural distortion in a given crystal structure, such as the perovskite LaMnO$_3$. Possible orbital ordering in a AMnX$_2$O$_6$ pyroxene with JT-active Mn^{3+} (3d^4) ions could result in rich magnetic properties. However, limited information on such compounds is available, with only the crystal structure of NaMnSi$_2$O$_6$ prepared under high-pressure and high-temperature conditions.[29] Motivated to have a thorough study of the structure−property relationships in a JT-active pyroxene, we synthesized the new pyroxene-type compound NaMnGe$_2$O$_6$ under 3 GPa and 800 °C and studied its crystal and magnetic structures and physical properties with X-ray single-crystal diffraction, neutron powder diffraction, and measurements of magnetic properties and specific heat. Like other alkali-metal pyroxenes with $S > 1/2$, we found that NaMnGe$_2$O$_6$ also undergoes a long-range AFM ordering below T_N = 7 K as a result of the interchain coupling. However, specific-heat measurements demonstrated that the short-range spin correlations within chains are evident at temperatures far above T_N. Moreover, due to the presence of competing AFM and FM exchange interactions, the compound undergoes a magnetic-field-driven spin-flip transition from AFM to a weak ferromagnetic state with a sufficiently high magnetic field. The observed magnetic behaviors are different from the prediction of the LSDA+U calculation.[3] Our present study completes the evolution of magnetic properties of the alkali-metal pyroxenes as a function of d-orbital occupancy from d^1 to d^5.

2. EXPERIMENTAL DETAILS

2.1. Sample Preparation. Polycrystalline NaMnGe$_2$O$_6$ samples were prepared under high-pressure and high-temperature (HPHT) conditions in a Walker-type, multianvil module. The precursor for the HPHT experiments was obtained via the conventional solid-state reaction of a stoichiometric mixture of Na$_2$CO$_3$, Mn$_2$O$_3$, and GeO$_2$ powders at 800 °C for 24 h in air. The precursor was contained in a gold capsule (i.d. = 1.68 mm and L = 3.0 mm). The gold capsule was

put into a BN sleeve and then inserted into a cylindrical graphite heater, both ends of which were contacted with molybdenum disks and steel rings. Other spaces were filled with pyrophyllite plugs. A semisintered Ceramacast 584 (5 wt % Cr$_2$O$_3$) octahedron served as pressure medium. In a typical HPHT experiment, the octahedron was first compressed to the desired pressure by eight truncated tungsten carbide cubes with the truncated edge length (TEL) = 8 mm. Then the sample was heated at 800 °C for 30−60 min before quenching to room temperature. Finally, the pressure was released slowly. The recovered samples were first examined with powder X-ray diffraction (XRD) at room temperature with a Philips X'pert diffractometer (Cu Kα radiation). The XRD data were collected by step-scanning from 15 to 80° in 2θ with an increment of 0.02° and a counting time of 10 s at each step.

2.2. Single-Crystal X-ray Diffraction. Small single crystals of dimensions up to 0.1 × 0.1 × 0.1 mm^3 were obtained from the products of high-pressure syntheses with a reaction time more than 60 min at 800 °C. Single-crystal X-ray diffraction data were collected at 153 K from a single crystal coated with mineral oil with Mo Kα radiation, λ = 0.710 73 Å, in a Rigaku SCX-Mini diffractometer equipped with a graphite monochromator. Structure refinement was carried out with the program SHELXL97 implemented in the program suite WinGX v1.80.05.

2.3. Magnetic Susceptibility and Specific Heat Measurements. The magnetic properties were measured with a commercial superconducting quantum interference device (SQUID) magnetometer from Quantum Design. The temperature dependences of magnetic susceptibility $\chi(T)$ under external magnetic fields of H = 0.1, 0.5, 1, and 5 T were measured in the temperature range 1.8−300 K after being zero-field-cooled (ZFC) and field-cooled (FC). We have also measured the magnetic susceptibility in the temperature range 300−750 K under a magnetic field of H = 1 T upon both heating up and cooling down. The magnetization $M(H)$ loops between 0 and 5 T were recorded at various temperatures T = 2, 5, 10, 15, and 20 K after ZFC. The specific heat $C(T)$ data were collected with a physical property measurement system (PPMS, Quantum Design) in the temperature range 1.9−200 K under magnetic fields up to 12 T.

2.4. Neutron Powder Diffraction Measurement. Our HPHT synthesis yields ∼25 mg of NaMnGe$_2$O$_6$ powder per run. Two neutron diffraction experiments were performed to determine the magnetic structure in the magnetically ordered phase below 7 K. Approximately 50 mg polycrystalline samples were first measured by use of the nanoscale-ordered materials diffractometer (NOMAD) at the Spallation Neutron Source (SNS), at Oak Ridge National Laboratory. NOMAD is one of the few available neutron diffractometers that allow the study of magnetism for a very small size sample. The powder was sealed in a vanadium can under helium atmosphere and cooled with an orange cryostat. Data were collected at selected temperatures below and above T_N (T = 2, 4, 6, 8, 12, and 25 K). The typical counting time is 6 h for each temperature point. Data from an empty sample can were collected and subtracted as background. While NOMAD measurements allow a quick determination of magnetic order parameter with a 50 mg powder sample, the data do not have good statistics for magnetic structure refinement. To solve this problem, more powder samples were synthesized and a ∼500 mg sample was measured again by using the HB2A diffractometer at several selected temperatures between 1.5 and 25 K. Rietveld refinements were carried out with the FULLPROF programs.

3. RESULTS

3.1. Phase Stability. All efforts to synthesize the pyroxene-type NaMnGe$_2$O$_6$ at ambient pressure result in a mixture of Na$_4$Ge$_9$O$_{20}$ and Mn$_2$O$_3$ phases. Redhammer et al.[30] have obtained an aenigmatite-type Na$_2$(Mn$_{5.26}$Na$_{0.74}$)Ge$_6$O$_{20}$ with mixed-valent Mn(II/III) by using the high-temperature flux growth method. We were left with a choice of the solid-state reaction under HPHT conditions, in analogy to the synthesis of NaMnSi$_2$O$_6$,[29] which was obtained at 1200 °C under 6 GPa for 24 h. However, we found that the single-phase NaMnGe$_2$O$_6$

can be obtained only within a very narrow temperature range. For $T \geq 1000$ °C, the product consists of GeO_2 and an unknown phase. On the other hand, the impurity phase $Na_2(Mn_{5.26}Na_{0.74})Ge_6O_{20}$ appears if the sintering temperature is lower than 800 °C. We obtained the nearly single-phase $NaMnGe_2O_6$ pyroxene at 850 ± 50 °C under a moderate pressure of 3 GPa for 30−60 min. Small single crystals of dimensions up to $0.1 \times 0.1 \times 0.1$ mm^3 were obtained in the high-pressure product if the holding time of heating was 60 min or longer.

3.2. Crystal Structure. The polycrystalline $NaMnGe_2O_6$ sample recovered from the HPHT synthesis is brown in color as the pellet was crushed into powder. The powder XRD pattern shown in Figure 2 can be indexed in a monoclinic unit cell with $a = 9.851(1)$ Å, $b = 8.758(1)$ Å, $c = 5.583(1)$ Å, and
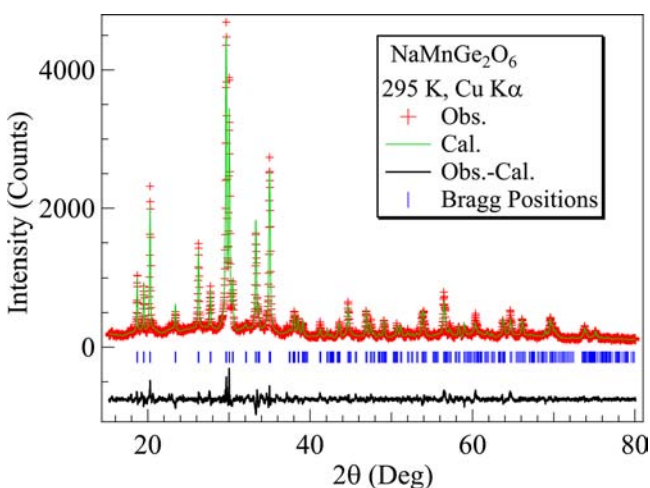

Figure 2. Observed (+), calculated (solid line), and difference (bottom line) XRD profiles of the $NaMnGe_2O_6$ powder sample after Rietveld refinement. The Bragg positions are shown by vertical bars.

$\beta = 105.51(1)$°. We have refined the XRD pattern by taking the structure of $NaMnSi_2O_6$ as a starting structural model,[29] which is defined in the $C2/c$ space group with Na and Mn atoms at the 4e $(0, y, ^1/_4)$ site, Ge atom at the 8f (x, y, z) site, and the three oxygen atoms at the 8f position. Although the result of the refinement in Figure 2 looks good, the obtained atom positions, especially for oxygen, came with very large error bars, which prevent a reliable structural analysis. Therefore, we carried out X-ray diffraction on a small single crystal with dimensions of about $0.02 \times 0.02 \times 0.02$ mm^3 and refined its crystal structure. Detailed information about the structural refinement is summarized in Table 2. The obtained atomic coordinates and the isotropic thermal parameters are presented in Table 3. Selected interatomic distances and bond angles are given in Table 4. The unit-cell crystal structure of $NaMnGe_2O_6$ is displayed in Figure 1a,b projected from the crystallographic c and b directions, respectively. The local oxygen-coordination polyhedra of the Na, Mn, and Ge atoms, together with some prominent structural features, are highlighted in Figure 1c.

The refinement of single-crystal XRD confirms that $NaMnGe_2O_6$ crystallizes into a monoclinic $C2/c$ structure with unit-cell parameters $a = 9.859(2)$ Å, $b = 8.7507(18)$ Å, $c = 5.5724(11)$ Å, and $\beta = 105.64(3)$° at room temperature. The lattice parameters are close to those determined from powder X-ray diffraction. The crystal structure of $NaMnGe_2O_6$ is isomorphous with other alkali-metal pyroxenes. As shown in

Table 2. Crystal Data and Structure Refinement for $NaMnGe_2O_6$ Single Crystal

empirical formula	Ge_2MnNaO_6
crystal system, space group	monoclinic, $C2/c$
unit-cell dimensions	
a (Å)	9.859(2)
b (Å)	8.7507(18)
c (Å)	5.5724(11)
β (deg)	105.64(3)
volume (Å^3), Z	462.96(16), 4
density (calcd) (mg/m^3)	4.578
formula wt	319.11
temp (K)	153
wavelength (Å)	0.710 73
absorption coeff (mm^{-1})	15.631
$F(000)$	592
crystal size (mm)	$0.02 \times 0.02 \times 0.02$
θ range for data collection (deg)	3.17−27.47
limiting indices	$-12 \leq h \leq 12, -11 \leq k \leq 11, -7 \leq l \leq 7$
reflns collected/unique	2377/536
R_{int}	0.0348
refinement method	full-matrix least-squares on F^2
data/restraints/parameters	536/0/47
goodness-of-fit on F^2	1.18
final R indices $[I > 2\sigma(I)]$	$R_1 = 0.0247$, w$R_2 = 0.0497$
R indices (all data)	$R_1 = 0.0281$, w$R_2 = 0.0505$
largest different peak, hole (e·Å^{-3})	0.582, −0.668

Figure 1, MnO_6 octahedra are connected with each other via screw edge-sharing, forming one-dimensional infinite chains parallel to the crystallographic c axis. A Mn−Mn chain is highlighted by connected bonds in blue in Figure 1c. These chains made of edge-shared octahedra are bridged by nonmagnetic GeO_4 tetrahedra, which also form a one-dimensional zigzag chain through corner sharing. The sodium atoms occupy the channels formed by these infinite chains. The MnO_6 octahedra are highly distorted, with three distinct Mn−O bond lengths of 1.918 Å (short), 1.991 Å (medium), and 2.198 Å (long), and the two longer bonds form a ~180° O−Mn−O bond connecting the two neighboring octahedra. As highlighted in Figure 1c by bonds in black, these long bonds in neighboring octahedra are parallel to each other, forming a long-range structural distortion along the chain direction. On the other hand, the medium Mn−O bonds form an in-chain right angle O−Mn−O link. The short Mn−O bonds always share an oxygen with Na and Ge. Such a distorted octahedron reflects that the single e_g electron of Mn^{3+} ($t_{2g}^3e_g^1$) occupies the $3z^2 - r^2$ orbital directed along the longest Mn−O bond. A structural distortion similar to this has also been observed in the sister compound $NaMnSi_2O_6$.[29] However, the Mn−Mn separation of 3.196 Å in $NaMnGe_2O_6$ is slightly longer than that of 3.131 Å in $NaMnSi_2O_6$ because of the larger Ge atoms. The GeO_4 tetrahedron shows a relatively small distortion with Ge−O distances ranging from 1.725 Å for Ge−O3 to 1.768 Å for Ge−O2. The average ⟨Ge−O⟩ bond length of 1.746 Å is consistent with the ionic radii sum for Ge^{4+} (0.390 Å) and O^{2-} (1.40 Å).[31] Within a coordination sphere of 2.6 Å, the Na atom is surrounded by six oxygen atoms with Na−O distances varying in the range from 2.341 Å for Na−O1 to 2.561 Å for Na−O3. Two O2 atoms are separated from the Na atom by 2.804 Å. Thus, the Na atom is 6-fold coordinated. The average

Table 3. Atomic Coordinates and Equivalent Isotropic Displacement Parameters for NaMnGe$_2$O$_6$

atom	method[a]	x	y	z	U_{eq}[b] (10^{-2} Å^2)
Na	XRD	0.5	−0.3003(3)	0.25	0.7(1)
	NPD	0.5	−0.29881(149)	0.25	0.2
Mn	XRD	0.5	0.08948(10)	0.25	0.4(1)
	NPD	0.5	0.08767(151)	0.25	0.2
Ge	XRD	0.29124(5)	−0.59302(5)	0.24134(8)	0.6(1)
	NPD	0.29181(46)	−0.59051(45)	0.24285(80)	0.5
O1	XRD	0.6080(3)	−0.0800(3)	0.1501(6)	1.0(1)
	NPD	0.60786(55)	−0.08043(67)	0.15225(96)	0.113(161)
O2	XRD	0.3642(3)	−0.5102(4)	0.0188(5)	0.9(1)
	NPD	0.36161(51)	−0.51214(76)	0.01442(118)	0.256(150)
O3	XRD	0.6402(3)	0.2257(3)	0.1917(6)	1.2(1)
	NPD	0.63625(54)	0.22434(55)	0.19007(101)	0.148(155)

[a]XRD, single-crystal X-ray diffraction at 153 K; NPD, neutron powder diffraction at 25 K. [b]U_{eq} is defined as a third of the trace of the orthogonalized U_{ij} tensor.

⟨Na−O⟩ bond length of 2.444 Å is in agreement with the ionic radii sum for Na$^+$ (1.02 Å) and O^{2-} (1.40 Å).[31]

The neutron powder diffraction patterns with good statistics were collected at 3 and 25 K, respectively. No observable structural change was detected upon crossing the magnetic transition. The nuclear structure data obtained from Rietveld refinement of the neutron diffraction data at 25 K are listed in Tables 3 and 4. The data are generally in line with the single-crystal X-ray results.

3.3. Magnetic Properties. The temperature dependence of magnetization M/H of NaMnGe$_2$O$_6$ was measured upon heating up from 2 to 300 K after ZFC and/or FC under different magnetic fields H = 0.1, 0.5, 1, and 5 T. The M/H curves above 30 K fully overlap with each other. To show clearly the low-temperature transition, Figure 3a displays only the M/H data below 50 K. Under a low magnetic field H = 0.1 T, M/H exhibits a sharp peak at T_N = 7 K, which indicates a long-range AFM ordering of the spin chains due to the interchain coupling. The ZFC and FC M/H curves bifurcate slightly at T < 5 K. On the other hand, the M/H curves under high magnetic fields H = 1 and 5 T, behave like those expected for a ferromagnet; the reduction of M/H under 5 T relative to that of 1 T is also consistent with the occurrence of a FM-like transition. The magnetic-field-induced transformation from an AFM to a FM state in NaMnGe$_2$O$_6$ is examined by further magnetization and specific-heat measurements.

We found that the inverse magnetic susceptibility $\chi^{-1}(T)$ of the paramagnetic phase at T < 300 K cannot be described well with a Curie−Weiss (C−W) law, $\chi = C/(T − \theta_w)$; however, the C−W law can be utilized to independently describe the temperature ranges 10−100 and 100−300 K in Figure 3. A C−W fit to $\chi^{-1}(T)$ in the temperature range 100−300 K yields an effective moment μ_{eff} = 4.94μ_B/Mn^{3+} and a Weiss temperature θ_w = −2.4 K, whereas the same fit between 10 and 100 K gives μ_{eff} = 4.82μ_B/Mn^{3+} and θ_w = +2.8 K. Both values of μ_{eff} are very close to the expected spin-only value, 4.9μ_B; the opposite sign of θ_w from the fitting in the different temperature range may suggest a gradual crossover from AFM coupling to FM interactions as temperature decreases. Alternatively, the $\chi^{-1}(T)$ curve in the whole paramagnetic region from 10 to 300 K can

be described excellently with a modified C−W law, $\chi = \chi_0 + C/(T − \theta_w)$, as shown by the solid line in Figure 3b; it yields a constant χ_0 = 4.35 × 10^{-4} emu/mol, μ_{eff} = 4.80μ_B/Mn^{3+}, and θ_w = +2.94 K.

The temperature dependence of magnetic susceptibility above room temperature was measured up to 750 K under a magnetic field of H = 1 T in both warming and cooling processes. As shown in Figure 3c, paramagnetic behavior was observed in the whole temperature range, and the magnetic susceptibility measured during cooling agrees well with that measured upon warming. This agreement indicates that NaMnGe$_2$O$_6$ is stable up to 750 K. The absence of any anomaly in the temperature dependence of magnetic susceptibility indicates no orbital order−disorder transition at T < 750 K. Results of fitting $\chi^{-1}(T)$ at T > 300 K agree well with that measured at T < 300 K.

The magnetization M(H) curves of ZFC NaMnGe$_2$O$_6$ measured between 0 and 5 T at various temperatures T = 2, 5, 10, 15, and 20 K are displayed in Figure 4. For the M(H) curves at 2 and 5 K, a clear anomaly can be seen at H_{sf} ≈ 0.5−0.6 T from the dM/dH versus H plot, as shown in the inset of Figure 4. Since the field-induced canting should evolve gradually as a function of magnetic field, the anomaly at H_{sf} ≈ 0.5−0.6 T is likely related to a spin-flipping transition. The obviously concave curvature of the M(H) curves at H > H_{sf} indicates a predominant ferromagnetic phase, which is consistent with the FM-like M(T) curves at H = 1 and 5 T in Figure 3a. On the other hand, the M(H) curves at T > T_N are not exactly linear, but exhibit a gradual slope change as shown in Figure 4. Similar M(H) behaviors have been reported in the compound NaCrSi$_2$O$_6$,[20] which is located right at the crossover from AFM LiCr(Si,Ge)$_2$O$_6$ to FM NaCrGe$_2$O$_6$. Therefore, the M(H) curves in Figure 4 indicate the presence of competing in-chain AFM and FM interactions in NaMnGe$_2$O$_6$; the compound behaves like an antiferromagnet at low fields, but a sufficiently high magnetic field stabilizes a ferromagnetic spin arrangement. Specific-heat measurements under different magnetic fields further confirm the analysis.

3.4. Specific Heat. The temperature dependence of specific heat $C(T)$ of NaMnGe$_2$O$_6$, measured under various magnetic fields up to 12 T, is shown in Figure 5. At zero field, $C(T)$

Table 4. Selected Bond Lengths and Angles of NaMnGe$_2$O$_6$^{a}

Bond Lengths (Å)			Bond Angles (deg)		
	XRD	NPD		XRD	NPD
NaO$_8$ Polyhedron			MnO$_6$ Octahedron		
Na–O1	2.341(4)	2.3176(11)	O1–Mn–O1^b	83.7 (2)	83.71(11)
Na–O1^b	2.341(4)	2.3176(11)	O1–Mn–O1^e	80.7(1)	81.16(7)
Na–O2	2.429(3)	2.4690(13)	O1–Mn–O1^f	96.1(1)	96.38(5)
Na–O2^b	2.429(3)	2.4690(13)	O1–Mn–O3	87.2(1)	87.85(7)
Na–O2^c	2.805(3)	2.7972(11)	O1–Mn–O3^b	167.1(1)	168.12(13)
Na–O2^d	2.805(3)	2.7972(11)	O1^b–Mn–O1^e	96.1(1)	96.38(5)
Na–O3^e	2.561(3)	2.5457(6)	O1^b–Mn–O1^f	80.7(1)	81.16(7)
Na–O3^f	2.561(3)	2.5457(6)	O1^b–Mn–O3^b	87.2(1)	87.85(7)
⟨Na–O⟩	2.534	2.5324	O1^b–Mn–O3	167.1(1)	168.12(13)
MnO$_6$ Octahedron			O1^e–Mn–O1^f	175.7(2)	176.72(4)
Mn–O1	1.991(3)	1.9718(14)	O1^e–Mn–O3	91.5(1)	90.55(9)
Mn–O1^b	1.991(3)	1.9718(14)	O1^e–Mn–O3^b	91.2(1)	91.52(6)
Mn–O1^e	2.198(3)	2.2105(5)	O3–Mn–O1^f	91.2(1)	91.52(6)
Mn–O1^f	2.198(3)	2.2105(5)	O3–Mn–O3^b	103.2(2)	101.64(14)
Mn–O3	1.918(3)	1.8900(16)	O3^b–Mn–O1^f	91.5(1)	90.55(9)
Mn–O3^b	1.918(3)	1.8900(16)	GeO$_4$ Tetrahedron		
⟨Mn–O⟩	2.036	2.024	O1^g–Ge–O2	111.0 (1)	110.45(13)
GeO$_4$ Tetrahedron			O1^g–Ge–O2^c	111.5(1)	111.36(11)
Ge–O1^g	1.743(3)	1.7459(19)	O1^g–Ge–O3^h	116.0(1)	115.68(14)
Ge–O2	1.750(3)	1.7403(9)	O2–Ge–O3^h	108.8(2)	107.54(9)
Ge–O2^c	1.767(3)	1.7355(10)	O2–Ge–O2^c	105.1(1)	107.06(5)
Ge–O3^h	1.725(3)	1.7651(8)	O2^c–Ge–O3^h	103.7(1)	104.24(10)
⟨Ge–O⟩	1.746	1.7466			
			Mn–O1–Mn1^e	99.3(1)	98.84(5)
Mn–Mn^e	3.19(10)	3.1803(6)			
Mn–Mn^i	3.1962(10)	3.1803(6)			

^{a}XRD, single-crystal X-ray diffraction at 153 K; NPD, neutron powder diffraction at 25 K. Symmetry transformations used to generate equivalent atoms are given in the respective footnotes. ^{b}(1 − x, y, 0.5 − z). ^{c}(x, −y − 1, z + 0.5). ^{d}(1 − x, −y − 1, −z). ^{e}(1 − x, −y, −z). ^{f}(x, −y, 0.5 + z). ^{g}(x − 0.5, y − 0.5, z). ^{h}(1 − x, y − 1, 0.5 − z). ^{i}(1 − x, −y, 1 − z).

exhibits a relatively broad λ-shaped anomaly peaked at $T = 7.18$ K, which is in excellent agreement with the magnetic-transition temperature T_N reflected at 0.1 T shown in Figure 3a. As shown in Figure 5, application of $H < H_{sf}$ has little influence on $C(T)$. On the other hand, with $H > H_{sf}$, the $C(T)$ anomaly at T_N becomes diminished and spreads over a much wider temperature range. Two features in the $C(T)$ data are noteworthy: (1) The high-temperature tail of the λ-shaped anomaly at zero field extends to a much higher temperature ($\gg 2T_N$) than those observed in a typical second-order magnetic transition of 3D magnets, suggesting the presence of strong short-range spin correlations far above the long-range magnetic-ordering temperature. Such a characteristic of low-dimensional magnets has also been observed in other sodium transition-metal pyroxenes.[28] (2) The dramatic effect of magnetic field on the $C(T)$ anomaly is in sharp contrast with the behavior in the Fe-based pyroxenes, such as LiFeGe$_2$O$_6$,[25] in which application of 9 T magnetic field makes a negligible modification on the $C(T)$ anomaly associated with a long-range AFM ordering. For $H > H_{sf}$, the magnetic-field effect on $C(T)$ of NaMnGe$_2$O$_6$ resembles those observed in typical ferromagnetic insulators, for example, EuO[32] and BiMnO$_3$.[33] This comparison indicates that NaMnGe$_2$O$_6$ is transformed into a predominant ferromagnetic phase under a large external magnetic field, which is consistent with the χ^{-1} versus T and M versus H results shown in Figures 3 and 4.

In order to calculate the magnetic entropy associated with the Mn^{3+} spins, we obtained the magnetic contribution $C_m(T)$ by subtracting the lattice part C_{lat} from the total $C(T)$. C_{lat} (solid line in Figure 5) is simulated in the temperature range 60–200 K with one Debye and two Einstein components with $\Theta_D = 387(8)$ K and $\Theta_E = 199(12)$ and 638(19) K, respectively. The resultant $C_m(T)$ and the corresponding magnetic entropy S below 50 K are shown in Figure 6. The experimental S value in the range 12.5–13.0 J/(mol·K), depending on the magnetic field applied from $H = 0$ to 12 T, accounts for about 93–97% of the expected magnetic entropy $S_{exp} = R \ln (2S + 1) = 13.38$ J/(mol·K) for the Mn^{3+} ions ($S = 2$). Therefore, it validates the method of modeling the lattice contribution employed here. As can be seen in Figure 6, a majority of the magnetic entropy, 68% under zero field and 88% under $H = 12$ T, is released above the long-range magnetic-ordering temperature marked by the dotted vertical line. This is typical of a low-dimensional magnetic system and signals the buildup of strong short-range spin correlations within the Q1D Mn^{3+}-spin chains at temperatures far above the long-range magnetic ordering.

3.5. Neutron Diffraction. Magnetic reflections were observed at low temperatures in the diffraction patterns collected on both instruments. In order to determine the magnetic structure, the 25 K data collected on HB2A were first refined to check the nuclear crystal structure of NaMnGe$_2$O$_6$, and the neutron refinement results are consistent with the X-ray results shown in Tables 3 and 4. Figure 7a shows the low-temperature NPD pattern collected on HB2A together with the refinement results by considering both the magnetic and nuclear structure unit cell. The temperature dependence and order parameter of the strong magnetic peak $(1\ 1\ -1/2)$ are shown
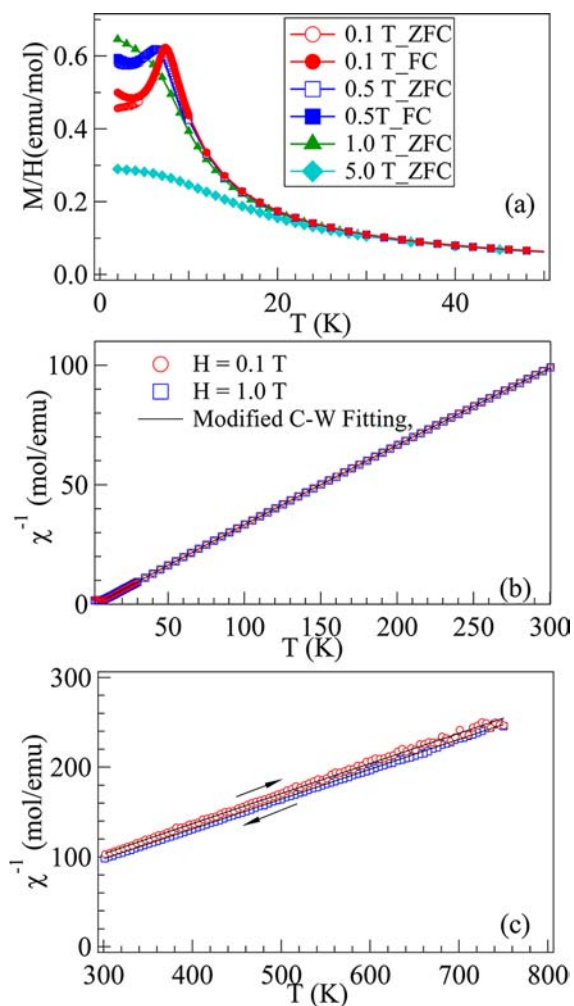
Figure 3. (a) Temperature dependence of the magnetization M/H of $NaMnGe_2O_6$ measured under different magnetic fields H = 0.1, 0.5, 1, and 5 T in the temperature range 2−60 K. (b) Temperature dependence of the inverse magnetic susceptibility $\chi^{-1}(T)$ in the temperature range 2−300 K. The solid line represents the modified Curie−Weiss fitting to the data from 10 to 300 K. (c) Temperature dependence of the inverse magnetic susceptibility $\chi^{-1}(T)$ of $NaMnGe_2O_6$ measured under a magnetic field of H = 1 T in the temperature range 300−750 K.

Figure 4. Magnetization M(H) curves of $NaMnGe_2O_6$ measured between 0 and 5 T at various temperatures T = 2, 5, 10, 15, and 20 K. The magnetic field of spin-flip transition, H_{fl} was defined from the maximum of the field derivative of magnetization dM/dH, shown in the inset.

Figure 5. Temperature dependence of specific heat $C(T)$ of $NaMnGe_2O_6$, measured under magnetic fields up to 12 T, presented in the form of C/T vs T (main panel) and C vs T (inset). The lattice contribution C_{lat}, shown as a solid line, is obtained by simulating the $C(T)$ data from 60 to 200 K with one Debye and two Einstein components.

in Figure 7 b,c. The order parameter data measured on NOMAD clearly shows that $NaMnGe_2O_6$ undergoes a long-range magnetic ordering transition at T_N = 7 K, which is in good agreement with the magnetic susceptibility and specific heat data. The observed magnetic peaks can be indexed with a propagation wave vector $(0\ 0\ ^1/_2)$ indicating the doubling of the magnetic unit cell along the c axis. A sketch of the refined magnetic structure is illustrated in Figure 7d; the magnetic moment of Mn^{3+} is aligned mainly along the c-axis with small component along both a and b axes as well; $m_a = 0.9(2)\mu_B$, $m_b = 0.4(4)\mu_B$, and $m_c = 1.8(1)\mu_B$. The refinement reveals a relatively smaller Mn^{3+} ordered moment of $1.92\mu_B$ at 3 K. The spin arrangements of the Mn moments yield an up−up−down−down spin structure along the chain direction c-axis, whereas the weak magnetic couplings between chains are ferromagnetic along both a and b axes. The up−up−down−down spin pattern indicates a spin-Peierls transition at T_N and reflects a competition between ferromagnetic and antiferromagnetic coupling along the chains.
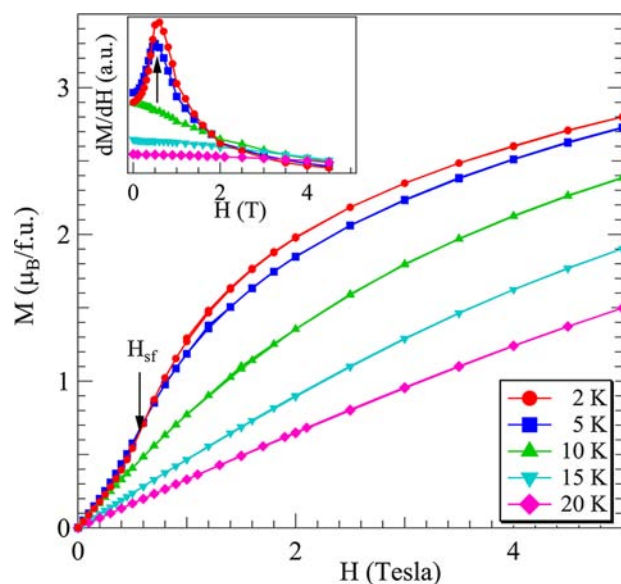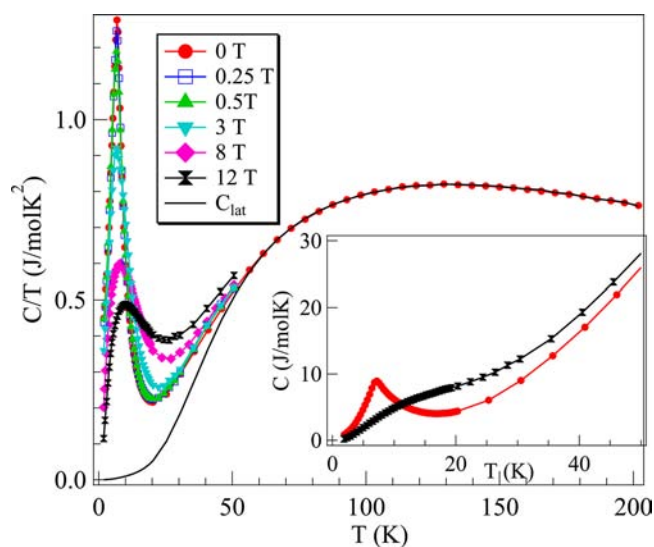
4. DISCUSSION

The fact that pyroxene minerals are commonly found in the Earth's crust indicates that it represents a group of chemicals in a high-density phase. However, HPHT synthesis is not necessary for most alkali pyroxenes. For example, the $NaTiSi_2O_6$ initially synthesized under HPHT conditions can also be obtained as a single phase at ambient pressure in an evacuated atmosphere.[4] Among all previously studied AMX_2O_6 compounds, HPHT synthesis is necessary only for synthesizing $NaMnSi_2O_6$.[30] As mentioned earlier, all our attempts were unsuccessful to synthesize Mn^{3+}-containing pyroxenes at
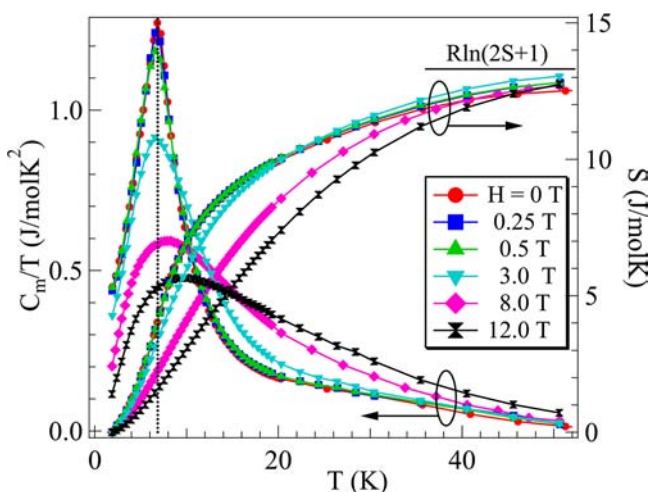
Figure 6. Temperature dependence of the magnetic contributions $C_m(T) = C - C_{lat}$ and the corresponding magnetic entropy under magnetic fields up to 12 T. The horizontal solid line marks the expected entropy value $R \ln (2S + 1)$ for Mn^{3+} ($S = 2$) ions, and the vertical dotted line marks the long-range magnetic ordering temperature.

ambient pressure with the solid-state reaction method by varying the reaction temperature, duration, and/or atmosphere. Instead, it seems that a moderate high-pressure condition is essential in order to stabilize the Mn^{3+} ions in the pyroxene structure, that is, $NaMnSi_2O_6$ at 6 GPa[29] and $NaMnGe_2O_6$ at 3 GPa. In well-studied perovskite or perovskite-related structures, high pressure is needed to alter the geometric tolerance factor in chemical combinations where the tolerance factor is out of the range in which the structure is stabilized.[34] In order to get insight into why high pressure is needed for the synthesis of Mn-based pyroxenes, we have to know the local distortion in the pyroxene structure. To measure quantitatively the local octahedral-site distortion, we used the bond-length distortion parameters[35] $\Delta_d \equiv (1/6)\sum_{i=1-6} (|d_i - \langle d \rangle|/\langle d \rangle)$ defined as the deviation of individual bond lengths d_i from their mean value $\langle d \rangle$. Figure 8 includes Δ_d values of known sodium pyroxenes $NaM(Si,Ge)_2O_6$ with M = Al, Cr, Ga, V, Fe, Mn, Ti, Sc, and In, which covers a broad range of ionic radii of M^{3+} ions.[36−39] All values of Δ_d for non-JT-active M^{3+} or weak JT ions like Ti^{3+} in an octahedral site are located around a line at $\Delta_d = 0.025$, which is significantly higher than $\Delta_d = 0.004$ found in the non-JT perovskite oxides.[40] The larger intrinsic octahedral-site distortion in the pyroxene structure originates from the asymmetric crystal-field environment, that is, edge-shared octahedra in chains instead of corner-shared octahedra forming a 3D framework in the perovskite structure. Moreover, edge-shared octahedra in chains also lead to O−Mn−O angles that deviate as much as 10° from the ideal 90°, whereas the deviation is normally smaller than 1° in the perovskite oxide.[41,42] The JT distortion in Mn^{3+}-based pyroxene only doubles Δ_d relative to that for non-JT pyroxenes; this difference is far less than that found in the manganite perovskites. In the orthorhombic perovskite oxides, the JT distortion essentially enlarges the intrinsic distortion of the crystal structure.[43,44] We can extract the intrinsic structural distortion of the pyroxene from the Sc^{3+}- and Ti^{3+}-based pyroxene in Figure 9. Whereas the bonding split is comparable to that in Mn^{3+}-based pyroxenes, the two long M-O bonds form a 90° angle at an octahedron in the non-JT pyroxene. In comparison, two long Mn−O bonds are located on the same direction, characteristic of orbital occupation at an octahedron in the Mn^{3+}-based pyroxene,

which means that the JT distortion competes with the intrinsic local distortion in the pyroxene structure. The JT distortion must be suppressed at high temperature and under high pressure in order for the Mn^{3+}-based pyroxene to form. Although the Ti^{3+} (t_{2g}^1) is also JT-active and its pyroxene compounds undergo a spin-Peierls-like transition associated with orbital ordering, the local octahedral-site distortion involving the t_{2g} electron is too small to be distinguished from the intrinsic structural distortion. A similar situation was also observed in the $RTiO_3$ (R = rare earth) perovskite.[45]

It is important to compare the local structural distortion in this new pyroxene $NaMnGe_2O_6$ with the prototype $LaMnO_3$ perovskite since both compounds have Mn^{3+} ions in octahedral sites. In both cases, the MnO_6 octahedron exhibits similar long−medium−short bond length distributions: 2.198, 1.991, and 1.918 Å in $NaMnGe_2O_6$ versus 2.183, 1.971, and 1.904 Å in $LaMnO_3$,[41] which gives a comparable bonding split Δ_d values of 5.3% versus 5.4%. The long-range cooperative orbital order competes with thermal fluctuations. In the perovskite $LaMnO_3$, the orbitally ordered state collapses at about $T_{JT} = 750$ K.[46] While no anomaly has been observed in the measurement of magnetic susceptibility at temperatures up to 750 K, we are in progress to explore a T_{JT} in pyroxene by studying the crystal structure at high temperatures up to the melting point or the decomposition temperature.

The syntheses of $(Li,Na)M(Si,Ge)_2O_6$ pyroxenes have been made successfully so far with the M^{3+} d^n configurations filled up to five 3d electrons. Co(III):d^6 at an octahedral site could have three spin states: low-spin (t^6e^0), intermediate-spin (t^5e^1), and high-spin (t^4e^2). The low-spin state has been confirmed in perovskites $RCoO_3$ (R = Nd, Sm, Eu, Gd, Tb, Dy). Co(III) in $LaCoO_3$ and $PrCoO_3$ undergoes a thermally driven spin-state transition to higher spin states. Co(III) in both the intermediate- and high-spin states is JT-active, but the JT distortion for high-spin Co(III) is very weak. The rhombohedral symmetry in the $LaCoO_3$ is not compatible with the cooperative long-range JT distortion for the intermediate-spin Co(III). However, $PrCoO_3$ has the orthorhombic structure and a recent neutron study has shown evidence of the intermediate-spin state.[47] The low-spin Co(III) has the smallest ionic radius among three spin states and prefers an undistorted or least-distorted octahedral site. The significantly high intrinsic distortion at the M^{3+} site in the pyroxene structure appears to favor the orbital ordering of the intermediate-spin state. However, as discussed above, the intrinsic site distortion of the pyroxene structure has the two long M−O bonds with a 90° angle, which is incompatible with the JT distortion. The failure to synthesize $(Li,Na)Co$-$(Si,Ge)_2O_6$ compounds under ambient pressure might signal the existence of JT distortion, that is, Co(III) ions are in intermediate-spin state, in Co^{3+}-based pyroxenes. Like the Mn^{3+}-based pyroxene in this work, high-pressure synthesis could be useful to alter this competition so as to stabilize a JT-active Co(III) in the pyroxene structure. If successful, the Co^{3+}-based pyroxene could be the best candidate for us to study the intermediate-spin Co(III).

After determining the local structural distortion, the possible orbital ordering at Mn^{3+} sites, and the magnetic structure resolved by neutron diffraction in $NaMnGe_2O_6$, we now turn to the microscopic picture of magnetic interactions. As illustrated in Figure 10, possible intrachain magnetic couplings include (1) direct exchange interaction through AFM t_{2g}−t_{2g}; (2) super-exchange interactions through the 90° Mn−O−Mn pathway AFM t_{2g}−O−t_{2g} and t_{2g}−O−e_g; and (3) exchange interaction
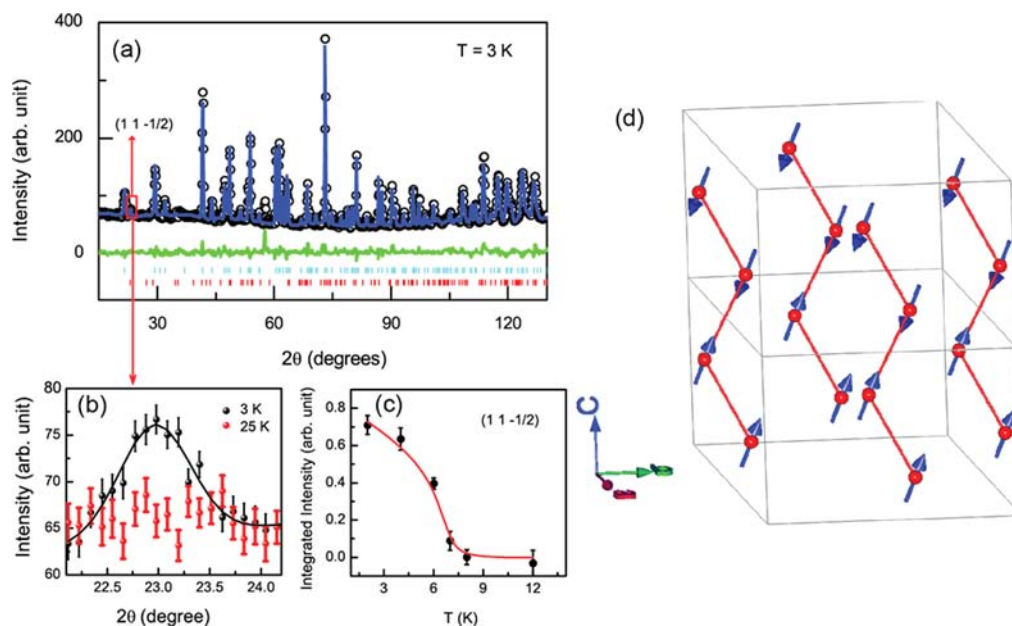
Figure 7. Neutron powder diffraction data of $NaMnGe_2O_6$ measured with NOMAD and HB2A diffractometers. (a) Observed NPD pattern ($\bigcirc$), calculated profile (solid line), and the difference (bottom line) measured at 3 K on HB2A. Vertical bars show the calculated nuclear and magnetic peak positions. The observed $(1\ 1\ -^1/_2)$ magnetic peak is highlighted. (b) $(1\ 1\ -^1/_2)$ magnetic peak at 3 and 25 K, measured on HB2A. (c) Magnetic order parameter of $(1\ 1\ -^1/_2)$ indicates the onset of AFM long-range-order transition at $T_N \approx 7$ K. The solid line is a guide for the eye. (d) Sketch of the determined magnetic structure of $NaMnGe_2O_6$ with a propagation wave vector $k = [0\ 0\ ^1/_2]$.

Figure 8. Octahedral-site bond length distortion parameter Δ_d of sodium pyroxenes $NaM(Si,Ge)_2O_6$ as a function of the ionic radius of M^{3+} ions.

of FM e_g–O–e_g through the orthogonal σ and π bonds on oxygen. A first-principles calculation by Streltsov and Khomskii[3] indicated that the AFM coupling ($J_{AFM} \sim 8.2$ K versus $J_{FM} \sim 4.8$ K) dominates the intrachain coupling. However, the new superlattice peak $(0,0,\ ^1/_2)$ of magnetic lattice below T_N and an up–up–down–down spin structure indicate that the microscopic picture outlined above is not complete. The space group used in the refinement gives a single O–Mn–O bond angle opening to the shared octahedral edge, that is, $\alpha = \beta = 80.6°$ in Figure 10. The FM e_g–O–e_g coupling is significantly reduced for $\alpha = \beta < 90°$. In contrast, the AFM t_{2g}–O–t_{2g} and t_{2g}–O–e_g are less sensitive to the bond angle. Therefore, one possibility to resolve this puzzle is to allow $\alpha \neq \beta$ in a structure with the subgroup of $C2/c$ below T_N. In this case, the FM e_g–O–e_g dominates in pairs of octahedra
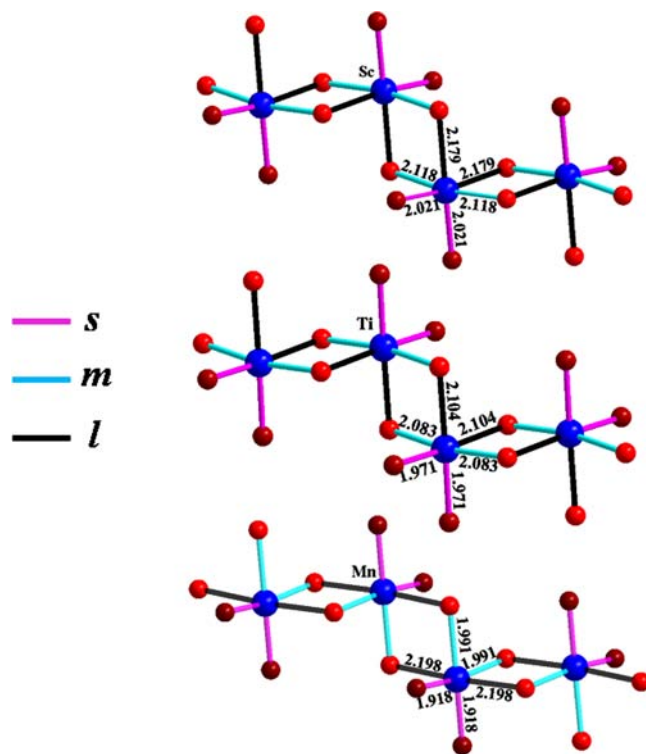

Figure 9. Schematic drawing of octahedra at the M site in the JT-inactive $NaScGe_2O_6$ (upper), weakly JT-active $NaTiSi_2O_6$ (middle), and JT-active $NaMnGe_2O_6$ (lower).

with O–Mn–O bond angle β close to 90°. Although the resolution of neutron diffraction we have made at $T < T_N$ is insufficient to resolve such a subtle structural modulation, our finding of new magnetic structure should stimulate further investigations.
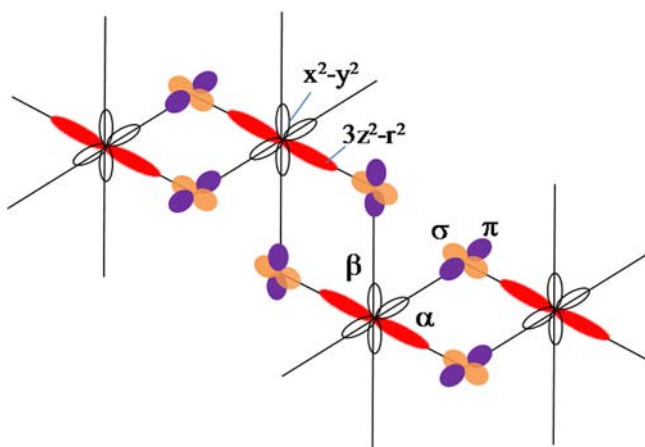
Figure 10. Schematic drawing of orbital ordering and local structure distortion. Hollow lobes are unoccupied orbitals. All occupied t_{2g} orbitals are not shown in the figure.

5. CONCLUSIONS

$NaMnGe_2O_6$ is the first example of a pyroxene with the e^1 configuration that has been thoroughly studied. The high-quality single-crystal diffraction provides reliable structural data for this new pyroxene. We have made a comparison between the structure for existing pyroxenes $(Li,Na)M(Ge,Si)_2O_6$ and the structural data in this work. The intrinsic octahedral-site distortion at the M site places two long M−O bonds at a 90° angle. While the bond length split defined by Δ_d is slightly larger for M = Mn than that in the JT-inactive pyroxenes, the JT distortion places two long Mn−O bonds in a line that is parallel with the direction of long Mn−O bonds in neighboring octahedra. Whereas the quasi-1D structural character leads normally to the Bonner−Fisher-like broad hump in para-magnetic susceptibility in some pyroxenes, $NaMnGe_2O_6$ exhibits a normal Curie−Weiss paramagnetic susceptibility and undergoes an antiferromagnetic transition at T_N= 7 K. However, a spin-flip transition from the AFM phase to a weak FM phase can be triggered by a modest magnetic field, which reflects a fragile balance between the AFM and FM couplings in the compound. The specific heat measurement indeed reveals that short-range spin fluctuations due to the quasi-1D structure exist at temperatures well above the Néel temperature. In contrast to the prediction from the first-principles calculation, the refinement of neutron powder diffraction below T_N reveals a spin ordering pattern of up−up−down−down along the c axis. A new structural model proposed below T_N remains to be confirmed by further studies.

■ AUTHOR INFORMATION

Corresponding Author
jqyan@utk.edu; jszhou@mail.utexas.edu
Notes
The authors declare no competing financial interest.

■ ACKNOWLEDGMENTS

■ REFERENCES

(1) Clark, J. R.; Appleman, D. E.; Papike, J. J. *Mineral. Soc. Am. Spec. Pap.* **1969**, *2*, 31.
(2) Jodlauk, S.; Becker, P.; Mydosh, J. A.; Khomskii, D. I.; Lorenz, T.; Streltsov, S. V.; Hezel, D. C.; Bohaty, L. *J. Phys.: Condens. Matter* **2007**, *19*, 432201.
(3) Streltsov, S. V.; Khomskii, D. I. *Phys. Rev. B* **2008**, *77*, 064405.
(4) Isobe, M.; Ninomiya, E.; Vasil'ev, A. N.; Ueda, Y. *J. Phys. Soc. Jpn.* **2002**, *71*, 1423.
(5) Ninomiya, E.; Isobe, M.; Ueda, Y.; Nishi, M.; Ohoyama, K.; Sawa, H.; Ohama, T. *Physica B (Amsterdam, Neth.)* **2003**, *329*, 884.
(6) Konstantinovic, M. J.; van den Brink, J.; Popovic, Z. V.; Moshchalkov, V. V.; Isobe, M.; Ueda, Y. *J. Magn. Magn. Mater.* **2004**, *272*, E657.
(7) Hikihara, T.; Motome, Y. *Phys. Rev. B* **2004**, *70*, No. 214404.
(8) van Wezel, J.; van den Brink, J. *J. Magn. Magn. Mater.* **2005**, *290*, 318.
(9) Millet, P.; Mila, F.; Zhang, F. C.; Mambrini, M.; Van Oosten, A. B.; Pashchenko, V. A.; Sulpice, A.; Stepanov, A. *Phys. Rev. Lett.* **1999**, *83*, 4176.
(10) Lou, J.; Xiang, T.; Su, Z. *Phys. Rev. Lett.* **2000**, *85*, 2380.
(11) Gavilano, J. L.; Mushkolaj, S.; Ott, H. R.; Millet, P.; Mila, F. *Phys. Rev. Lett.* **2000**, *85*, 409.
(12) Lumsden, M. D.; Granroth, G. E.; Mandrus, D.; Nagler, S. E.; Thompson, J. R.; Castellan, J. P.; Gaulin, B. D. *Phys. Rev. B* **2000**, *62*, R9244.
(13) Vonlanthen, P.; Tanaka, K. B.; Goto, A.; Clark, W. G.; Millet, P.; Henry, J. Y.; Gavilano, J. L.; Ott, H. R.; Mila, F.; Berthier, C.; Horvatic, M.; Tokunaga, Y.; Kuhns, P.; Reyes, A. P.; Moulton, W. G. *Phys. Rev. B* **2002**, *65*, No. 214413.
(14) Vasiliev, A.; Voloshok, T.; Ignatchik, O.; Isobe, M.; Ueda, Y. *JETP Lett.* **2002**, *76*, 30.
(15) Pedrini, B.; Gavilano, J. L.; Rau, D.; Ott, H. R.; Kazakov, S. M.; Karpinski, J.; Wessel, S. *Phys. Rev. B* **2004**, *70*, No. 024421.
(16) Vasiliev, A. N.; Ignatchik, O. L.; Isobe, M.; Ueda, Y. *Phys. Rev. B* **2004**, *70*, No. 132415.
(17) Isobe, M.; Ueda, Y. *J. Magn. Magn. Mater.* **2004**, *272−276*, 948.
(18) Pedrini, B.; Wessel, S.; Gavilano, J. L.; Ott, H. R.; Kazakov, S. M.; Karpinski, J. *Eur. Phys. J. B* **2007**, *55*, 219.
(19) Vasil'ev, A. N.; Ignatchik, O. L.; Sokolov, A. N.; Hiroi, Z.; Isobe, M.; Ueda, Y. *JETP Lett.* **2003**, *78*, 551.
(20) Vasiliev, A. N.; Ignatchik, O. L.; Sokolov, A. N.; Hiroi, Z.; Isobe, M.; Ueda, Y. *Phys. Rev. B* **2005**, *72*, No. 012412.
(21) Nenert, G.; Isobe, M.; Ritter, C.; Isnard, O.; Vasiliev, A. N.; Ueda, Y. *Phys. Rev. B* **2009**, *79*.
(22) Nenert, G.; Ritter, C.; Isobe, M.; Isnard, O.; Vasiliev, A. N.; Ueda, Y. *Phys. Rev. B* **2009**, *80*.
(23) Redhammer, G. J.; Roth, G.; Paulus, W.; Andre, G.; Lottermoser, W.; Amthauer, G.; Treutmann, W.; Koppelhuber-Bitschnau, B. *Phys. Chem. Mineral.* **2001**, *28*, 337.
(24) Ballet, O.; Coey, J. M. D.; Fillion, G.; Ghose, A.; Hewat, A.; Regnard, J. R. *Phys. Chem. Mineral.* **1989**, *16*, 672.
(25) Drokina, T.; Petrakovskiï, G.; Bayukov, O.; Bovina, A.; Shimchak, R.; Velikanov, D.; Kartashev, A.; Volkova, A.; Ivanov, D.; Stepanov, G. *Phys. Solid State* **2010**, *52*, 2405.
(26) Drokina, T.; Bayukov, O.; Petrakovskiï, G.; Velikanov, D.; Bovina, A.; Stepanov, G.; Ivanov, D. *Phys. Solid State* **2008**, *50*, 2141.
(27) Drokina, T.; Petrakovskiï, G.; Keller, L.; Schefer, J. *J. Phys.: Conf. Ser.* **2010**, *251*, No. 012016.

(28) Baker, P. J.; Lewtas, H. J.; Blundell, S. J.; Lancaster, T.; Franke, I.; Hayes, W.; Pratt, F. L.; Bohaty, L.; Becker, P. *Phys. Rev. B* **2010**, *81*, No. 214403.

(29) Ohashi, H.; Osawa, T.; Tsukimura, K. *Acta Crystallogr.* **1987**, *C43*, 605.

(30) Redhammer, G.; Roth, G.; Topa, D.; Amthauer, G. *Acta Crystallogr.* **2008**, *C64*, i21.

(31) Shannon, R. D. *Acta Crystallogr.* **1976**, *A32*, 751.

(32) Ahn, K.; Pecharsky, A. O.; Gschneidner, K. A. J.; Pecharsky, V. K. *J. Appl. Phys.* **2004**, *97*, No. 063901.

(33) Belik, A. A.; Takayama-Muromachi, E. *Inorg. Chem.* **2006**, *45*, 10224.

(34) Goodenough, J. B.; Kafalas, J. A.; Longo, J. M. High-Pressure Synthesis. In *Preparative Methods in Solid State Chemistry*; Academic Press, Inc.: New York and London, 1972.

(35) Renner, B.; Lehmann, G. *Z. Kristallogr.* **1986**, *175*, 43.

(36) Redhammer, G. J.; Ohashi, H.; Roth, G. *Acta Crystallogr. B* **2003**, *59*, 730.

(37) Genkina, E. A.; Maksimov, B. A.; Timofeeva, V. A.; Bykov, A. B. *J. Struct. Chem.* **1985**, *26*, 136.

(38) Redhammer, G. J.; Roth, G.; Amthauer, G. *Acta Crystallogr., Sect. C: Cryst. Struct. Commun.* **2008**, *64*, I97.

(39) Emirdag-Eanes, M.; Kolis, J. W. *Mater. Res. Bull.* **2004**, *39*, 1557.

(40) Zhou, J.-S.; Goodenough, J. B. *Phys. Rev. B* **2004**, *69*, No. 153105.

(41) Dabrowski, B.; Kolesnik, S.; Baszczuk, A.; Chmaissem, O.; Maxwell, T.; Mais, J. *J. Solid State Chem.* **2005**, *178*, 629.

(42) Kennedy, B. J.; Vogt, T.; Martin, C. D.; Parise, J. B.; Hriljac, J. A. *J. Phys.: Condens. Matter* **2001**, *13*, L925.

(43) Zhou, J.-S.; Goodenough, J. B. *Phys. Rev. Lett.* **2005**, *94*, No. 065501.

(44) Zhou, J.-S.; Goodenough, J. B. *Phys. Rev. B* **2008**, *77*, No. 132104.

(45) Cheng, J.-G.; Sui, Y.; Zhou, J.-S.; Goodenough, J. B.; Su, W. H. *Phys. Rev. Lett.* **2008**, *101*, No. 087205.

(46) Zhou, J.-S.; Goodenough, J. S. *Phys. Rev. B* **1999**, *60*, R15002.

(47) Ren, Y.; Yan, J.-Q.; Zhou, J.-S.; Goodenough, J. B.; Jorgensen, J. D.; Short, S.; Kim, H.; Proffen, T.; Chang, S.; McQueeney, R. J. *Phys. Rev. B* **2011**, *84*, No. 214409.

(48) Satto, C.; Millet, P.; Galy, J. *Acta Crystallogr., Sect. C: Cryst. Struct. Commun.* **1997**, *C53*, 1727.

(49) Ohashi, H.; Osawa, T.; Sato, A. *Acta Crystallogr., Sect. C: Cryst. Struct. Commun.* **1994**, *C50*, 1652.

(50) Redhammer, G. J.; Roth, G.; Treutmann, W.; Hoelzel, M.; Paulus, W.; André, G.; Pietzonka, C.; Amthauer, G. *J. Solid State Chem.* **2009**, *182*, 2374.